

Cluster bulleticity

Richard Massey,¹★ Thomas Kitching¹★ and Daisuke Nagai^{2,3}★

¹University of Edinburgh, Institute for Astronomy, Royal Observatory, Blackford Hill, Edinburgh EH9 3HJ

²Department of Physics, Yale University, New Haven, CT 06520, USA

³Yale Center for Astronomy and Astrophysics, New Haven, CT 06520, USA

Accepted 2010 December 20. Received 2010 December 20; in original form 2010 July 12

ABSTRACT

The unique properties of dark matter are revealed during collisions between clusters of galaxies, such as the bullet cluster (1E 0657–56) and baby bullet (MACS J0025–12). These systems provide evidence for an additional, invisible mass in the separation between the distributions of their total mass, measured via gravitational lensing, and their ordinary ‘baryonic’ matter, measured via its X-ray emission. Unfortunately, the information available from these systems is limited by their rarity. Constraints on the properties of dark matter, such as its interaction cross-section, are therefore restricted by uncertainties in the individual systems’ impact velocity, impact parameter and orientation with respect to the line of sight.

Here we develop a complementary, statistical measurement in which every piece of substructure falling into every massive cluster is treated as a bullet. We define ‘bulleticity’ as the mean separation between dark matter and ordinary matter, and we measure the signal in hydrodynamical simulations. The phase space of substructure orbits also exhibits symmetries that provide an equivalent control test.

Any detection of bulleticity in real data would indicate a difference in the interaction cross-sections of baryonic and dark matter that may rule out hypotheses of non-particulate dark matter that are otherwise able to model individual systems. A subsequent measurement of bulleticity could constrain the dark matter cross-section. Even with conservative estimates, the existing *Hubble Space Telescope* archive should yield an independent constraint tighter than that from the bullet cluster. This technique is then trivially extendable to and benefits enormously from larger, future surveys.

Key words: elementary particles – gravitational lensing: weak galaxies: clusters: general – cosmology: theory – dark matter – X-rays: galaxies: clusters.

1 INTRODUCTION

The standard Λ cold dark matter (Λ CDM) cosmological model includes a component of CDM that amounts to 85 per cent of the matter content of the Universe. This dark matter affects the Universe primarily through gravity and is necessary to explain the distribution and growth of large-scale structure over cosmic time. However, dark matter does not interact (or only very weakly) in the electroweak sector.

The fundamentally different properties of dark matter and baryonic matter are highlighted most dramatically in their temporary separation during collisions between galaxy cluster pairs, such as 1E 0657–56 (Clowe Gonzalez & Markevitch 2004; Bradač et al. 2006; Clowe et al. 2006) and MACS J0025–12 (Bradač et al. 2008). These ‘bullet clusters’ have provided astrophysical constraints on

the interaction cross-section σ of hypothesized dark matter particles and may ultimately prove the most useful laboratory in which to test for any velocity dependence of the cross-section. Unfortunately, the utility of a small number of individual systems is limited by observational uncertainties in their collision velocity, impact parameter and angle with respect to the plane of the sky (Randall et al. 2008). Current constraints are 3 orders of magnitude weaker than constraints from the shapes of haloes (Feng 2010) and, since collisions between two massive progenitors are rare (Shan, Qin & Zhao 2010), the total observable number of such systems may be inadequate to investigate a physically interesting regime of dark matter properties.

In this paper, we present a statistical method that allows every piece of substructure falling into every cluster to contribute to a global measure of dark matter–baryonic separation that we refer to as ‘bulleticity’. In this approach, every infalling mass is treated as a bullet, whose (interacting) gas is expected to collide with the intracluster medium (ICM) and lag behind the (non-interacting) dark matter (Powell, Kay & Babul 2009). Although offsets between

★E-mail: rm@roe.ac.uk (RM); tdk@roe.ac.uk (TK); daisuke.nagai@yale.edu (DN)

baryonic gas (e.g. as seen in X-ray emission) and total mass (e.g. as seen by gravitational lensing) may not be *individually* significant, detecting a mean bulleticity across many systems would provide robust evidence for a difference between the baryonic matter and dark matter interaction cross-sections. Measurements of the *amplitude* of bulleticity could then constrain the level of the dark matter–dark matter and dark matter–baryonic cross-sections. Crucially, since bulleticity should be observable in the ongoing assembly of every massive structure throughout the Universe, our statistical technique can overcome the previous limitations of small number statistics.

This paper is organized as follows. In Section 2, we develop a simple physical model to illustrate the concept of bulleticity and explore some of its dependencies. In Section 3, we use full hydrodynamical calculations to measure the expected bulleticity signal in realistic galaxy clusters. In Section 4, we discuss the practicality of measurements from real astronomical data and use a Fisher matrix analysis to predict constraints on the interaction cross-section of dark matter using various data sets. We conclude in Section 5.

2 DYNAMICAL MODEL

2.1 Motion of test particles falling into clusters

We shall illustrate the dominant physical effects that separate components of dark and baryonic mass as they fall into a massive cluster. Throughout, we shall refer to the combined infalling system as a ‘bullet’.

Consider the rest frame of a cluster with fixed ‘singular isothermal sphere’ 3D mass distribution $\rho(r) = \rho_0(r_0/r)^2$, which has a mass interior to radius r of $M(<r) = 4\pi\rho_0 r_0^2 r$. An infalling, point-like component at position \mathbf{r} , which interacts only gravitationally, has an equation of motion:

$$\frac{d^2\mathbf{r}}{dt^2} = -\frac{4\pi G\rho_0 r_0^2}{r^2}\mathbf{r}, \quad (1)$$

where t is the proper time for the cluster and r is the 3D radius.

An equivalent component that also interacts via the electroweak force experiences additional pressure support. We approximate this interaction as a buoyancy force equal to the weight of the displaced mass. For a sufficiently small bullet that the density $\rho(r)$ of the cluster is constant across it, the equation of motion is

$$\frac{d^2\mathbf{r}}{dt^2} \approx -\frac{4\pi G\rho_0 r_0^2}{r^2} \left[1 - (137\alpha)^2 \frac{\rho_0 r_0^2}{\rho_b r^2} \right] \mathbf{r}, \quad (2)$$

where α is the dimensionless coupling constant and ρ_b is the mean (total) density of the bullet, assuming that the ratio of baryons to dark matter is the same in the cluster and the bullet.

We shall use equation (1) with $\alpha = 0$ to model the dynamics of standard CDM and equation (2) with $\alpha = 1/137$ to model baryonic matter. To study interacting dark matter, we can simply add a non-zero α term, which represents the mean of the dark matter–dark matter and dark matter–baryonic coupling constants, weighted by the ratio in which the two forms of matter are found in the cluster. Such particles would follow orbits between those of standard dark matter and baryons. The $(137\alpha)^2$ prefactor can be interpreted as either the fractional volume of cluster mass displaced by a solid bullet or the fractional cross-section seen by an interacting particle, i.e. for a geometrically thin bullet $(137\alpha)^2 \approx \sigma/\pi r_b^2$.

Note that both dark and baryonic matter also experience dynamical friction and tidal gravitational forces but equally, so that neither of these effects separate the two components. To keep our model simple, we therefore ignore these effects but note that the dissipation

of the bullet due to tidal and ram-pressure stripping, in conjunction with the finite crossing time of a typical cluster, means that we would only ever expect to see bullets on their first one or two passes through a cluster. Whilst the dynamical friction of a lumpy ICM would begin to circularize the bullet’s orbit during this time, we also neglect this effect.

2.2 Definition of bulleticity

We define bulleticity \mathbf{b} as the vector from the position of the dark matter, projected on to the plane of the sky, to that of the baryons. Its magnitude is thus sensitive to the difference $\Delta\sigma$ in the total interaction cross-sections of dark matter and baryons. Were all matter to have the same interaction cross-section, this would ensure $\mathbf{b} \equiv 0$. Any non-zero detection will therefore indicate the presence of non-baryonic material.

We define the location of the bullet to be the mean position (r, θ) of the dark matter and the baryons projected on to the sky. In general, these need not be the same. We need to uniquely define the location of each bullet because its bulleticity can depend upon the length of time it has been within a cluster and the path it has previously traversed. Henceforth, we shall use the symbol r to represent this 2D projected radius.

In the 1D case of a bullet that falls into a cluster potential along a radius, equations (1) and (2) both produce oscillatory motion (with the caveat of a numerical finesse at the origin to remove the point of infinite density). However, as the baryons experience extra buoyancy, they gradually lag behind the dark matter: farther from the cluster core during infall and closer to the core during egress. The absolute bulleticity $b = |\mathbf{b}|$ steadily increases.

The 2D orbit of a bullet with a non-zero impact parameter but in the plane of the sky is illustrated in Fig. 1. In this calculation, we assume a cluster of mass $10^{14} M_\odot$ within $0.8 h^{-1}$ Mpc and adopt a value of $\rho_b = 10^6 M_\odot (h^{-1} \text{ kpc})^{-3}$ for the baryons; the resulting bulleticity is inversely proportional to this value. To show the bulleticity more clearly, the trajectory is extended to include several passes through the cluster, during each of which the separation of dark and baryonic matter visibly increases. At each point along the mean trajectory, the green line in the bottom panel shows the absolute bulleticity $b(r)$. During the first infall, the separation gradually increases, with baryons lagging behind dark matter as in the 1D case. On each subsequent pass, the two components separate at large radii, as they follow different trajectories, but return to each other as they near the cluster core.

The bulleticity vector can be conveniently written in terms of components that are radial b_r and azimuthal b_t with respect to the centre of the cluster, such that

$$\mathbf{b} = b_r \hat{\mathbf{e}}_r + b_t \hat{\mathbf{e}}_t, \quad (3)$$

where $\hat{\mathbf{e}}_r$ and $\hat{\mathbf{e}}_t$ are unit vectors. This is illustrated in Fig. 4 later in the text. While the radial and tangential bulleticity components are smaller than the absolute bulleticity $b = |\mathbf{b}|$, the crucial point is that they are signed. When averaging over all possible viewing angles or the phase space of possible bullet orbits, the mean tangential separation averages to zero (it can be easily demonstrated in this case by switching the handedness of the orbit to produce a mirror image of Fig. 1). Such symmetries ensure that, for a large sample of bullets, $\langle b_t \rangle \equiv 0$. The remaining, non-zero component of radial bulleticity b_r is shown in Fig. 1 as a grey line.

We thus propose two complementary bulleticity estimators. The absolute bulleticity b is positive definite, so it is likely to provide the first detection of a difference in the behaviour of dark and baryonic

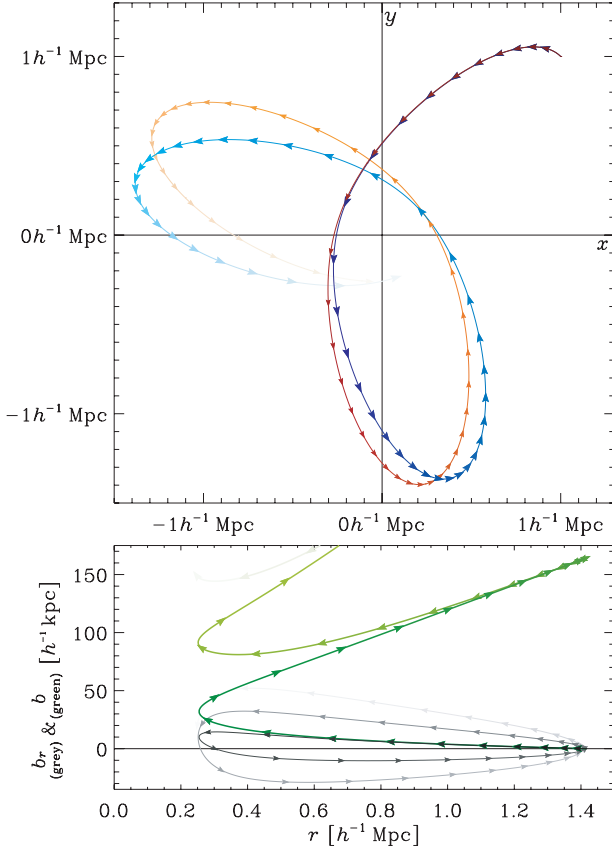


Figure 1. Orbits of test particles falling into a $10^{14} M_{\odot}$ ‘singular isothermal sphere’ cluster. In the top panel, the blue curve (large arrows) shows the trajectory of standard, non-interacting $\alpha = 0$ CDM, which is governed in this simple model purely by the gravitational attraction from the central mass. The red curve (small arrows) shows the trajectory of $\alpha = 1/137$ baryonic matter, which experiences an additional buoyancy force. Arrowheads are spaced uniformly in proper time, and the paths progressively fade. The bottom panel shows the apparent bulleticity if the substructure is moving in the plane of the sky.

matter at a relatively large signal-to-noise ratio (S/N). The radial bulleticity b_r has a smaller signal, but subsequent measurements from a large cluster sample will benefit from its corresponding statistical check for systematics, b_t . This latter combination should eventually provide the method’s cleanest constraints on the interaction cross-section of dark matter.

2.3 Robustness to astrophysical variation

The distribution of mass in the cluster affects the orbits of a bullet. As shown in Fig. 2, dark matter precesses around a cuspy mass (converging to Keplerian orbits in the limit of a point-like central mass, with the mass at one focus of the ellipse), but has constant elliptical orbits around a cored cluster, with the centre of the mass at the centre of the ellipse. Importantly, however, for a fixed impact parameter, the bulleticity of substructure on its first pass through a cluster changes by less than 5 per cent for a wide range of cluster profiles. This lack of influence means that, to first order, uncertainty about the unknown mass distribution can be ignored, and one can freely average results from a large ensemble of clusters. It also means that bulleticity measurements are unlikely to constrain the density profile of galaxy clusters. However, other methods are ex-

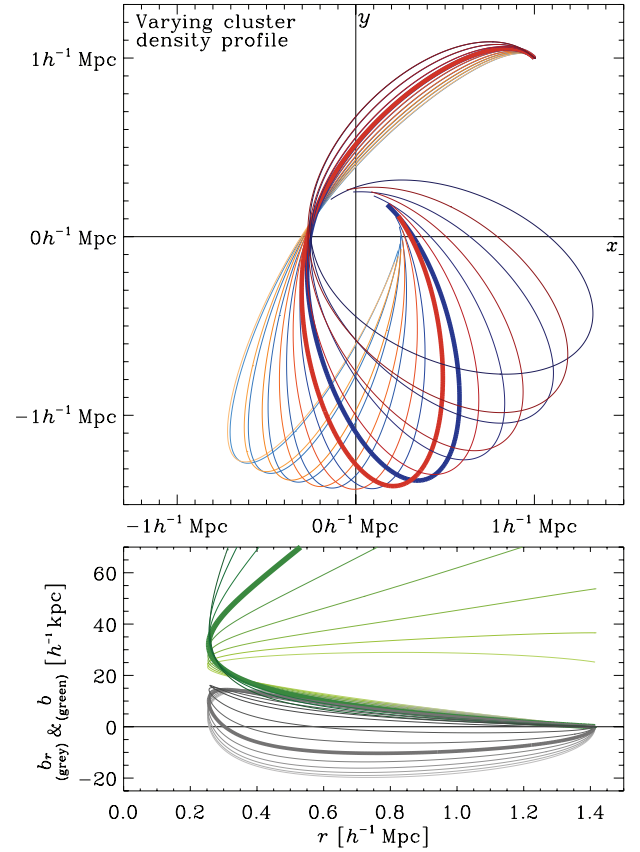


Figure 2. Varying the power-law slope of the density profile $\rho \propto r^{-\gamma}$ between $\gamma = -1$ (light) and $\gamma = -2.6$ (dark) in steps of 0.2, for a fixed cluster mass and bullet density, while adjusting the bullet’s initial velocity to also ensure a constant impact parameter. Note that b/γ is small around $\gamma = -2$ (thick line). To avoid confusion, the orbits are only traced up to the second periapsis (point of closest approach) and bulleticity to the second apoapsis.

pected to constrain this independently (Massey Kitching & Richard 2010).

Conversely, varying a bullet’s impact parameter does affect its subsequent bulleticity. As shown in Fig. 3, baryons with a low impact parameter pass through more of the ICM, experience greater buoyancy and exhibit larger bulleticity after periapsis. Bullets with a low impact velocity accumulate a greater impulse from buoyancy, so they also have a higher bulleticity – especially in the tangential direction, i.e. $b_t \gg b_r$. Deriving quantitative predictions about the level of bulleticity expected in real clusters will therefore require integrations over the phase space of initial conditions and subsequent orbits in a typical cosmology, as well as detailed modelling of the growth and early infall of substructure. Such analysis is beyond our simple physical model. To do this properly, we shall now switch to full hydrodynamical calculations, which also automatically include the more subtle physical effects that we have disregarded so far.

3 FULL HYDRODYNAMICAL CALCULATION

3.1 Properties of the simulations

We shall now measure the bulleticity signal in realistic, high-resolution hydrodynamical simulations of massive clusters embedded in a standard cosmological model. The model is flat, with parameters $\Omega_m = 1 - \Omega_{\Lambda} = 0.3$, $\Omega_b = 0.04286$, $h = 0.7$ and

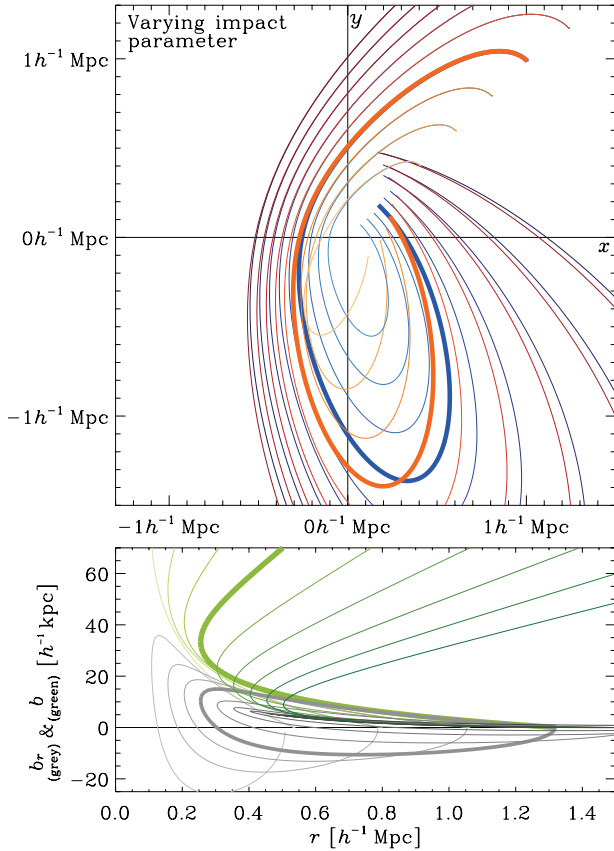


Figure 3. Changing the impact parameter from 100 to $500 h^{-1}$ kpc in steps of $50 h^{-1}$ kpc (while keeping the impact velocity and the cluster profile fixed). The default $250 h^{-1}$ kpc orbit is shown as a thick line. The orbit clearly has a more dramatic influence than the cluster's density profile (Fig. 2), so building a theoretical prediction for real clusters will clearly require an integration over initial phase-space conditions.

$\sigma_8 = 0.9$, where the Hubble constant is defined as $100 h \text{ km s}^{-1} \text{ Mpc}^{-1}$ and σ_8 is the mass variance within spheres of a radius of $8 h^{-1} \text{ Mpc}$. All distances are expressed in comoving coordinates.

We performed our simulations with the Adaptive Refinement Tree *N*-body+gasdynamics code (Kravtsov 1999; Kravtsov, Klypin & Hoffman 2002), which uses adaptive refinement in space and time, and (non-adaptive) refinement in mass (Klypin et al. 2001) to resolve high dynamic ranges. The spatial resolution in the cores of haloes is $\sim 6 h^{-1} \text{ kpc}$ and the particle mass is $3\text{--}9 \times 10^8 h^{-1} M_\odot$. The formation of galaxy clusters is followed from cosmological initial conditions through later properties of the ICM including gas cooling and star formation. Astrophysical processes in our simulations include metal enrichment and thermal feedback due to Type Ia and Type II supernovae, self-consistent advection of metals, metallicity-dependent radiative cooling and UV heating due to a cosmological ionizing background. Potentially relevant physical processes excluded from the simulations are active galactic nucleus bubbles, magnetic fields and cosmic rays, although these are most important in the innermost cluster regions, which we shall exclude anyway. More details about our simulations are available in Nagai, Kravtsov & Vikhlinin (2007a,b).

We realize simulated 2D observations of 16 independent clusters at two redshifts $z = 0.6$ and 0 by projecting snapshots of the dark matter density, gas density and gas temperature along three

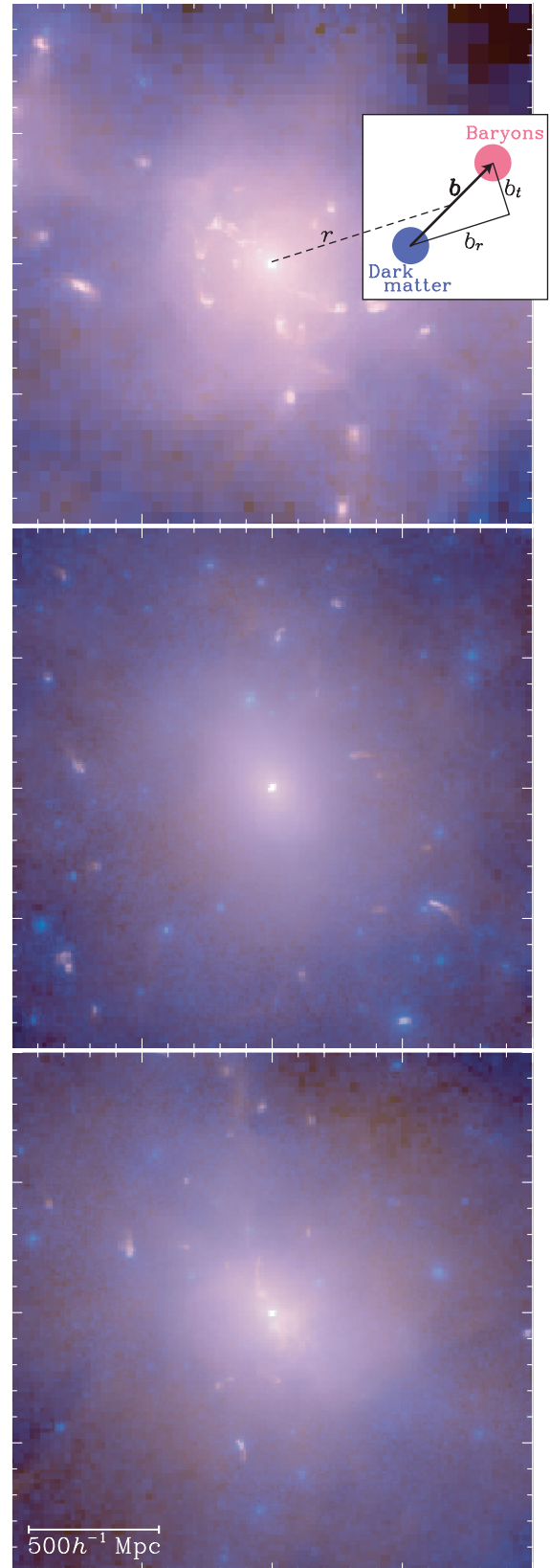


Figure 4. Full hydrodynamical simulations of massive clusters at redshift $z = 0.6$. Blue shows total projected mass (dominated by dark matter) and red shows X-ray emission from baryonic gas. The preferential trailing of gas due to pressure from the ICM, and its consequent separation from the non-interacting dark matter, is apparent in much of the infalling substructure.

Table 1. Mean properties of the simulated clusters.

	N_{cluster}	N_{bullet}	Mass M_{500} ($10^{14} M_{\odot}$)	Size r_{500} (h^{-1} Mpc)
Redshift $z = 0.6$				
All	48	1142	1.2 ± 0.2	0.75 ± 0.05
Relaxed	16	303	1.6 ± 0.5	0.79 ± 0.09
Unrelaxed	32	839	1.0 ± 0.2	0.68 ± 0.04
Redshift $z = 0$				
All	48	1079	2.9 ± 0.6	0.73 ± 0.06
Relaxed	27	453	2.0 ± 0.6	0.66 ± 0.07
Unrelaxed	21	626	3.6 ± 0.9	0.79 ± 0.08

orthogonal axes. This produces 48 cluster realizations at each redshift, some of which are illustrated in Fig. 4. Like the simulations by Powell et al. (2009), ours show complex interactions of substructure. Mock *Chandra* X-ray imaging was used to visually classify each projection as either relaxed or unrelaxed (Nagai, Vikhlinin & Kravtsov 2007a). The cluster masses M_{500} span a range of about an order of magnitude centred on $10^{14} M_{\odot}$, and Table 1 lists the mean mass M_{500} , size r_{500} and number of bullets N_{bullet} in several sub-samples, where the size of a cluster is defined as the radius of a sphere in which the mean density is 500 times the critical density of the Universe at that epoch.

3.2 Analysis of the simulations

We apply unsharp masking to maps of both the lensing mass and the baryonic gas density squared times the square root of the temperature (equivalent to the X-ray emission only if it is due to thermal bremsstrahlung, but the rest of our analysis is completely robust to this simplification). We then find the best-fitting Gaussian to every local maximum via the iteration in size and position adopted by Rhodes Réfrégier & Groth (2000). This algorithm is robust but may not be optimal in the regime of real observational noise and beam smearing. Even in our noiseless simulations, measurements near the cluster core are hindered by the steep background gradient from central emission, particularly in the X-ray signal, which pulls the best-fitting peak inwards. More sophisticated algorithms might prevent this, such as simultaneous fitting of all the sources (cf. Marshall 2006). However, we circumvent the issue by ignoring the (very few) peaks within $200 h^{-1}$ kpc of the cluster centre. We cross-match X-ray peaks to their nearest lensing peak projected within $0.5 h^{-1}$ Mpc, then apply the match the other way around and keep only uniquely defined pairs.

Figs 5 and 6 show the observed mean separation between the centres of matched X-ray and lensing peaks, projected within $0.5 h^{-1}$ Mpc on the sky and averaged over all subpeaks. The radial and tangential components b_r and b_t can be positive or negative, so they partially cancel upon averaging, while $b \equiv \sqrt{b_r^2 + b_t^2}$ is positive definite for all bullets. As in Section 2, we define the centre of the bullet as the mean of the X-ray and lensing positions, and we compute the components of the bulleticity vector with respect to the direction towards the global minimum of the projected gravitational potential. As expected from the simple model in Section 2, the absolute bulleticity increases towards the centre of the cluster, reaching $26 h^{-1}$ kpc ≈ 4 arcsec at $r = 0.3 r_{500}$ and $z = 0.6$. The normalization is independent of the cluster mass (at both redshifts), within a 1σ uncertainty of $4 h^{-1}$ kpc per order of magnitude in mass. The measurements are well fitted by cubic polynomials

$$b(r) = \frac{\Delta\sigma}{\pi r_b^2} (b_0 + b_1 r + b_2 r^2 + b_3 r^3), \quad (4)$$

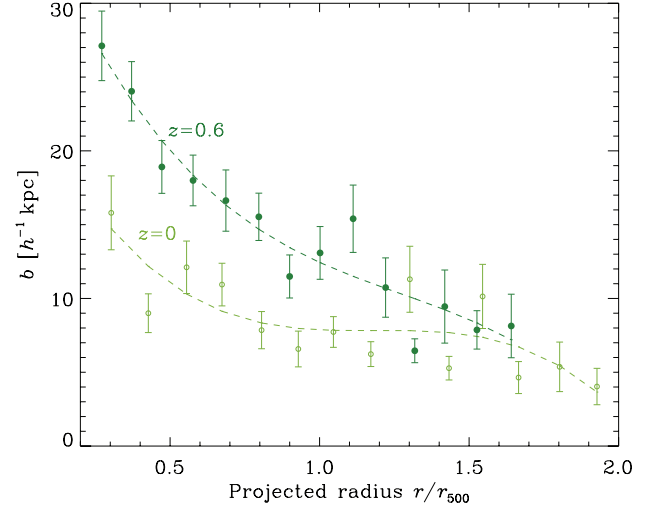


Figure 5. Measurements of absolute bulleticity from full hydrodynamical simulations. Error bars show 1σ errors. Dashed lines are best-fitting cubic polynomials to guide the eye. As expected for orbits in which only the first crossing has been completed, bulleticity increases as the infalling group falls towards the cluster centre and the gas is preferentially retarded.

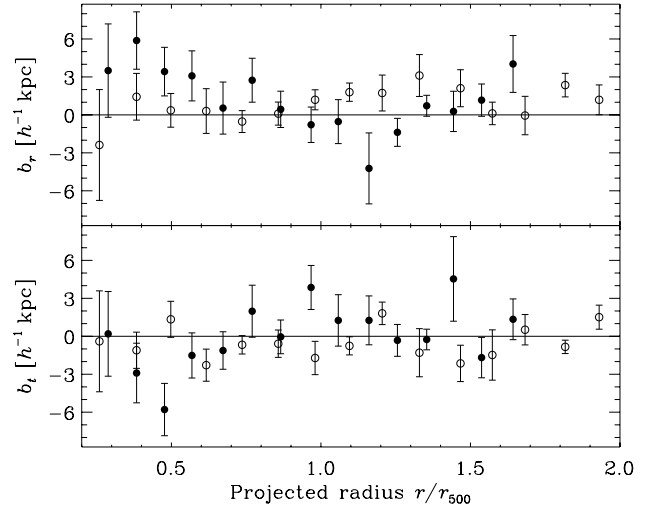


Figure 6. Measurements of radial and tangential bulleticity from full hydrodynamical simulations. These quantities are signed so, once averaged over many clusters, the values are smaller than those in Fig. 5. Filled circles show data from redshift $z = 0.6$ and open circles show data from $z = 0$. The only significant detection is of radial bulleticity $b_r(r < r_{500}) = 1.7 \pm 0.7 h^{-1}$ kpc at $z = 0.6$. The mean tangential bulleticity is consistent with zero, demonstrating its utility as a control test in this harder but potentially more discriminating measurement.

where the coefficients $b_i = \{38.2, -51.6, 35.0, -9.2\}$ at $z = 0.6$ and $b_i = \{24.7, -43.0, 36.4, -10.3\}$ at $z = 0$, assuming a fiducial model in which the prefactor is unity. If the polynomial order is increased, the quartic coefficients are an order of magnitude lower.

The radial and tangential bulleticity signals are an order of magnitude lower and noisier. The only statistically significant detection is that $\langle b_r \rangle = 1.7 \pm 0.7 h^{-1}$ kpc within r_{500} at $z = 0.6$. This too appears independent of cluster mass, and all other measurements are consistent with zero. In particular, the fact that the tangential

bulleticity signal is always consistent with zero demonstrates its utility as a control test for any observational systematics.

3.3 Dependence upon redshift

The bulleticity signal decreases between the two cosmic epochs we have studied. An explanation for this, in agreement with our predictions from the simple model of Section 2, is that the masses of clusters are considerably lower at $z = 0.6$. With a correspondingly lower infall velocity, the baryons therefore experience a larger impulse from buoyancy. Furthermore, high-redshift clusters are also generally more disturbed, have more substructures per unit mass and have larger offsets between central dark matter and gas peaks. However, the projected angle of b on the sky *increases* for nearby clusters. Were the absolute bulleticity to decline linearly with proper time between the values measured at redshifts $z = 0.6$ and 0, the expectation of $b(0.3 r_{500})$ would rise in angular size to ~ 10 arcsec at $z = 0.1$ and ~ 16 arcsec at $z = 0.05$.

Clusters at low redshift will make the best targets for observation. As well as their increasing bulleticity signal, nearby clusters also provide a more optimal geometry for gravitational lensing. The common misconception to the contrary may have arisen from Hamana Takada & Yoshida (2004), who detected peaks using a matched filter of fixed 1 arcmin size. Nearby clusters appear larger than this on the sky, so their fixed filter produces a diminishing signal below $z \sim 0.3$. A better matched filter reveals that the signal is larger, but merely spread thin (Kubo et al. 2007, 2009). Finally, massive, low-redshift clusters should contain more substructure. The fact that our sample includes a similar amount of substructure at all redshifts is probably a selection effect because our high-redshift clusters are the most massive progenitors of present-day structures; as a result, they are growing rapidly.

3.4 Dependence upon environment

None of the bulleticity signals show a statistically significant dependence upon the cluster's apparent dynamical state. However, at redshift $z = 0.6$ (0), unrelaxed clusters yielded about 1.4 (1.8) times as many bullets per cluster as relaxed clusters, despite having slightly lower masses at $z = 0.6$. For this measurement, unrelaxed clusters might therefore provide more profitable targets.

We also tried stacking bulleticity measurements from different clusters in terms of the bullets' absolute distance from the cluster centre, rather than as a fraction of r_{500} . Because the cluster sizes vary little within our sample, the qualitative result does not change.

In particularly crowded regions of clusters, it would be possible to mismatch pairs of dark matter- and baryonic-projected peaks from different substructures. However, this confusion effect will dampen the measured bulleticity and, if it is a function of cluster radius, it will be most pronounced towards the centre, where the separation is largest and the density of bullets is highest. If the aim is purely to detect bulleticity b in order to prove the existence of dark matter, this effect will therefore only make the measurement more difficult rather than producing a spurious signal.

4 PRACTICALITY OF A REAL MEASUREMENT

So far, we have maximally exploited our computationally expensive simulations by not adding noise to our mass or X-ray maps. We shall now consider the likelihood of and practical issues that will be faced by any real measurement of bulleticity.

Baryonic substructure is frequently seen in deep *Chandra* imaging (e.g. Gastaldello et al. 2009; Randall et al. 2009). Dark matter substructure can be mapped efficiently via strong gravitational lensing or flexion (Goldberg & Bacon 2005; Bacon et al. 2006), which probes gradients in the mass distribution and is therefore more sensitive to small mass peaks along a line of sight than weak shear. Coe et al. (2011) resolved 10 previously unknown subpeaks at various radii within the (unrelaxed) cluster A1689 using strong lensing, and Leonard et al. (2007) and Leonard, King & Goldberg (2011) resolved four using flexion. Both of these measurements were made independently of the distribution of light.

Combined X-ray and gravitational lensing observations have already revealed a separation of baryons from dark matter in two real systems undergoing major mergers. In the bullet cluster 1E0657–56, Clowe et al. (2006) measured separations of $b = 49.3$ arcsec $= 152 h^{-1}$ kpc (main cluster) and 46.1 arcsec $= 142 h^{-1}$ kpc (bullet). In MACS J0025.4–1222, Bradač et al. (2008) measured separations of dark matter from the central gas peak of $b = 49.3$ arcsec $= 228 h^{-1}$ kpc (south-east clump) and 30.1 arcsec $= 139 h^{-1}$ kpc (north-west clump). While these measurements have small errors, it is their interpretation that remains difficult. The extreme disruption of these systems has removed any well-defined global potential minimum, so it is difficult to place the substructure at a well-defined radius r or to split the bulleticity into components b_r and b_t . Minor merger events will be more usual targets for bulleticity.

Noise in a real measurement – whether due to a finite exposure time for X-ray observations or a finite source density of lensed background galaxies – will create scatter in the measured peak positions. This will emerge as a constant minimum b signal. Indeed, this effect is tentatively seen as a value around $6 h^{-1}$ kpc at large r in Fig. 5, which coincides with the resolution limit of the simulations. A resolution limit will be especially problematic in clusters at high redshift, although statistical techniques more sophisticated than an offset between peaks will inevitably help. For example, the cross-correlation between the full lensing and X-ray maps could be measured. Most importantly, measurements of the (signed) radial and tangential bulleticity from a large cluster sample will beat down noise on $\langle b_r \rangle$ and ensure that $\langle b_t \rangle \rightarrow 0$.

To predict the observable bulleticity signal, we assume that substructure positions can be resolved to $6 h^{-1}$ kpc, which is achievable with *Chandra* at $z < 0.3$. At radii where the expected bulleticity signal (4) is resolved, we assume that the observed rms error $\sigma_b(r)$ falls from the baseline of Fig. 5 as $1/\sqrt{N_b}$, where N_b is the number of bullets. Once the approved Multi-Cycle Treasury programme ‘Through a lens, darkly’ (P.I. Postman) has been performed, the *Hubble Space Telescope* (HST)/Advanced Camera for Surveys (ACS) imaging archive will include ~ 50 clusters between redshifts $z = 0.1$ and 0.2. If these clusters contain just ~ 100 substructure peaks, and even exclude measurements of those within the central $200 h^{-1}$ kpc, they should provide a detection of $b(r)$ at an S/N of ~ 11 when integrated over scales of $6 h^{-1}$ kpc $< r < 2 r_{500}$. The *Euclid* survey (Massey et al. 2004; Réfrégier et al. 2010) should yield a similar detection significance for $b_r(r)$ and $b_t(r)$, even if only one substructure peak is identified in each of its $\sim 40\,000$ clusters within the same redshift range.

We can estimate the tightness with which such measurements will constrain the dark matter interaction cross-section using the Fisher information matrix (Tegmark Taylor & Heavens 1997). We again adopt the best-fitting models of $b(r)$ from equation (4), interpolating linearly with proper time between $z = 0.6$ and 0, and baseline observational noise $\sigma_b(r)$ around that shown in Fig. 5. We assume

that the bulleticity in radial bins is uncorrelated and note that the dependence on $\Delta\sigma$ is in the mean of $b(r)$ (not the covariance). In this case, the one-parameter Fisher information is

$$F = \sum_{\text{bullets}} \sum_r \frac{1}{\sigma_b^2(r)} \left[\frac{\partial b(r)}{\partial \Delta\sigma} \right]^2$$

$$= \sum_{\text{bullets}} \frac{1}{(\pi r_b^2)^2} \sum_r \frac{(b_0 + b_1 r + b_2 r^2 + b_3 r^3)^2}{\sigma_b^2(r)}. \quad (5)$$

We have summed equally over r bins where $r > 200 h^{-1}$ kpc and $b(r) > 6 h^{-1}$ kpc, but this could be generalized to incorporate a more sophisticated weight function that increases the overall S/N. For the observational scenarios described above, $F(\pi r_b^2)^2 \sim 100$ for the *HST* archive and $\sim 30\,000$ for *Euclid*.

Notably, equation (5) does not depend on the fiducial value of $\Delta\sigma$. With a more comprehensive suite of hydrodynamical simulations to more accurately model the behaviour of baryonic substructure, we could therefore directly interpret constraints on $\Delta\sigma$ as those on σ . Assuming typical bullets of mass $m_b \sim 5 \times 10^{12}$ and radius $r_b \sim 10 h^{-1}$ kpc, we thus predict 68 per cent confidence limits of

$$\left(\frac{\sigma}{m} \right) = \frac{1}{m_b \sqrt{F}} \sim \begin{cases} 1 \times 10^{-25} \text{ cm}^2 \text{ GeV}^{-1} & \text{for } HST \\ 6 \times 10^{-27} \text{ cm}^2 \text{ GeV}^{-1} & \text{for } Euclid. \end{cases} \quad (6)$$

Compare this to 68 per cent confidence limits from the bullet cluster of $\sigma/m < 1.25 \text{ cm}^2 \text{ g}^{-1} = 2 \times 10^{-24} \text{ cm}^2 \text{ GeV}^{-1}$ or $\sigma/m < 0.7 \text{ cm}^2 \text{ g}^{-1}$ assuming that the main cluster and sub-cluster had similar mass-to-light ratios prior to the merger (Randall et al. 2008).

Even with these fairly conservative estimates, we expect a bulleticity analysis of the *HST* archive to produce constraints on σ similar to or tighter than the bullet cluster. Furthermore, such constraints are potentially unlimited by the uncertainty in orbital parameters for any single object. The fundamental strength of our statistical method is the trivial way in which it can then be extended to exploit larger surveys such as *Euclid*. Bulleticity thus offers a path towards ever more discriminating measurements, even if individual extreme merger events turn out to be rare (Shan et al. 2010).

5 DISCUSSION

We have defined a measure of dark matter–baryonic matter separation ‘bulleticity’ that takes contributions from every detected substructure peak in every massive cluster. Any non-zero bulleticity measures the difference between the interaction cross-sections of dark and baryonic matter. This interesting new test can be understood via the intuition of a simple model, and we have also measured the expected value of the bulleticity signal using full hydrodynamical simulations of Λ CDM clusters.

A conservative estimate of currently available data and analysis techniques suggests that there should be enough information in clusters from the *HST* archive to detect bulleticity at an S/N greater than 10. With further hydrodynamical simulations to interpret the absolute level of the signal, this could yield independent constraints on the interaction cross-section of dark matter at a level similar to or tighter than the bullet cluster. The real strength of this method is the way in which it can subsequently exploit large future surveys, free of biases from individual systems and in a trivially expandable way. An ambitious, all-sky survey could thus rival constraints from particle physics experiments (Feng 2010). For a targeted survey, the ideal targets would include massive, low-redshift and possibly unrelaxed clusters. Most crucially, bulleticity measurements will be obtained

in a physical regime unapproachable in terrestrial laboratories and may ultimately provide the best test for any velocity dependence of the dark matter interaction cross-section.

As a final tantalizing prospect, we note that the positions of galaxies provide a third (and more easily measured) observable. Indeed, Randall et al. (2008) derived tighter constraints on the dark matter cross-section by comparing the post-collision locations of dark matter and galaxies (rather than dark matter and gas). To first order, galaxies pass straight through each other unimpeded because of the separation between them and between the stars in each galaxy. The vector from dark matter to galaxies is therefore a ‘bulleticity’ measured around a fiducial model of $\sigma = 0$, so it provides a more direct measurement of the non-zero interaction cross-section. There are still potential complications to this picture. For example, Russell et al. (2010) found a group of galaxies in A2146 leading the X-ray emission as expected, but the brightest cluster galaxy lags behind it. Complex baryonic physics can also affect observations: Cortese et al. (2007) showed that stars lead gas in galaxies that are merging into clusters, but that new star formation can also be triggered in the gas, with the new stars only gradually falling forwards into the main galaxy. If such effects can be theoretically modelled, the most practical tool for this measurement is likely to be strong gravitational lensing. If the positions of peaks in a standard *LensFit* mass reconstruction (e.g. Richard et al. 2010) were allowed to float instead of being tied to the positions of galaxies, their measured offsets would be precisely this new bulleticity.

ACKNOWLEDGMENTS

The authors would like to thank Patrick Simon, Ken Rice, Phil Marshall, Cathie Clarke, Justin Read, Johan Richard and James Taylor for conversations that spurred the development of this paper. It also benefited greatly from helpful suggestions by the anonymous referee. RM is supported by STFC Advanced Fellowship PP/E006450/1 and ERC grant MIRG-CT-208994. TK is supported by STFC rolling grant RA0888. DN acknowledges the support of Yale University and NSF grant AST-1009811.

REFERENCES

- Bacon D., Goldberg D., Rowe B., Taylor A., 2006, MNRAS, 365, 414
- Bradač M. et al., 2006, ApJ, 652, 937
- Bradač M., Allen S., Treu T., Ebeling H., Massey R., Morris G., von der Linden A., Applegate D., 2008, ApJ, 687, 959
- Clowe D., Gonzalez A., Markevitch M., 2004, ApJ, 604, 596
- Clowe D., Bradač M., Gonzalez A., Markevitch M., Randall S., Jones C., Zaritsky D., 2006, ApJ, 648, L109
- Coe D., Benitez N., Broadhurst T., Moustakas L., Ford H., 2011, ApJ, submitted (arXiv:1005.0398)
- Cortese L. et al., 2007, MNRAS, 376, 157
- Feng J., 2010, ARA&A, 48, 495
- Gastaldello F., Buote D., Temi P., Brighenti F., Mathews W., Ettori S., 2009, ApJ, 693, 43
- Goldberg D., Bacon D., 2005, ApJ, 619, 741
- Hamana T., Takada M., Yoshida N., 2004, MNRAS, 350, 893
- Klypin A., Kravtsov A., Bullock J., Primack J., 2001, ApJ, 554, 903
- Kravtsov A., 1999, PhD thesis, New Mexico State Univ.
- Kravtsov A., Klypin A., Hoffman Y., 2002, ApJ, 571, 563
- Kubo J., Stebbins A., Annis J., Dell’Antonio I., Lin H., Khiabani H., Frieman J., 2007, ApJ, 671, 1466
- Kubo J. et al., 2009 ApJ, 702, L110
- Leonard A., Goldberg D., Haaga J., Massey R., 2007, ApJ, 666, 51
- Leonard A., King L., Goldberg D., 2011, MNRAS, in press (doi:10.1111/j.1365-2966.2010.18171.x) (arXiv:1009.1018)

- Marshall P., 2006, MNRAS, 372, 1289
 Massey R. et al., 2004, AJ, 127, 3089
 Massey R., Kitching T., Richard J., 2010, Rep. Progress Phys. 73, 086901
 Nagai D., Vikhlinin A., Kravtsov A., 2007a, ApJ, 655, 98
 Nagai D., Kravtsov A., Vikhlinin A., 2007b, ApJ, 668, 1
 Powell L., Kay S., Babul A., 2009, MNRAS, 400, 705
 Randall S., Markevitch M., Clowe D., Gonzalez A., Bradač M., 2008, ApJ, 670, 1173
 Randall S., Jones C., Markevitch M., Blanton E., Nulsen P., Forman W., 2009, ApJ, 700, 1404
 Réfrégier A. et al., 2010, preprint (arXiv:1001.0061)
 Rhodes J., Réfrégier A., Groth E., 2000, ApJ, 536, 79
 Richard J. et al., 2010, MNRAS, 404, 325
 Russell H., Sanders J., Fabian A., Baum S., Donahue M., Edge A., McNamara B., O'Dea C., 2010, MNRAS, 406, 1721
 Shan H., Qin B., Zhao H., 2010, MNRAS, 408, 1277
 Tegmark M., Taylor A., Heavens A., 1997, ApJ, 480, 22

This paper has been typeset from a \TeX/L\AA\TeX file prepared by the author.